The Role of the Electrode Surface in Na–Air Batteries: Insights in Electrochemical Product Formation and Chemical Growth of NaO 2

Lukas Lutz, Daniel Alves Dalla Corte, Yuhui Chen, Dmitry Batuk, Lee R Johnson, Artem Abakumov, Luis Yate, Eneko Azaceta, Peter Bruce, Jean-marie Tarascon, et al.

Article type: Full Paper

Title: The role of the electrode surface in Na-air batteries; insights in electro-chemical product formation and chemical growth of NaO_2.

Lukas Lutz, Daniel Alves Dalla Corte, Yuhui Chen, Dmitry Batuk, Lee R. Johnson, Artem Abakumov, Luis Yate, Eneko Azaceta, Peter G. Bruce, Jean-Marie Tarascon and Alexis Grimaud*

Lukas Lutz, Dr. Daniel Alves Dalla Corte, Dr Alexis Grimaud*, Prof. Jean-Marie Tarascon
Chimie du Solide et de l'Energie, FRE 3677, Collège de France, 75231 Paris Cedex 05, France
*Email: alexis.grimaud@college-de-france.fr

Lukas Lutz, Dr. Yuhui Chen, Dr Lee Johnson, Prof. Peter G. Bruce
Department of Materials, University of Oxford, Parks Road, Oxford OX1 3PH, UK

Dr. Luis Yate
CIC biomaGUNE, Parque Tecnológico de San Sebastián, Paseo Miramón, 182.Ed., Empresarial C, 20014 San Sebastián (Guipúzcoa), SPAIN

Dr. Eneko Azaceta
IK4-CIDETEC, Parque Technologico de San Sebastian, P Miramon, 196, 20009 Donostia-San Sebastian, Spain

Dr. Dmitry Batuk,
EMAT, University of Antwerp, Groenenborgerlaan 171, B-2020 Antwerp, Belgium

Prof. Artem Abakumov
EMAT, University of Antwerp, Groenenborgerlaan 171, B-2020 Antwerp, Belgium
Skolkovo Institute of Science and Technology, *Moscow 143025, Russia*

Keywords: Na-air battery, Na-O_2 battery, NaO_2 growth, oxygen redox, electrode surface

Abstract:

The Na-air battery, because of its high energy density and low charging overpotential, is a promising candidate for low-cost energy storage, hence leading to intensive research. However, to achieve such a battery, the role of the positive electrode material in the discharge process must be understood. This issue is herein addressed by exploring the electrochemical reduction of oxygen, and the chemical formation and precipitation of NaO_2 using different electrodes. Whereas we demonstrate a minor influence of the electrode surface on the electrochemical formation of NaO_2, we identify a strong dependence of the subsequent chemical precipitation of NaO_2. In the origin, this effect stems from the surface energy and O_2/O_2^- affinity of the electrode. The strong interaction of Au with O_2/O_2^-, increases the nucleation rate and leads to an altered growth process when compared to C surfaces. Consequently, thin (3μm) flakes of NaO_2 are found on Au, whereas on C large cubes (10μm) of NaO_2 are formed. This has significant impact on the cell performance and leads to 4 times higher capacity when C electrodes with low surface energy and O_2/O_2^- affinity are used. We hope these findings will enable the design of new positive electrode materials with optimized surfaces.

1. Introduction

Research on non-aqueous metal-air batteries has drawn considerable attention over the last decade. Due to the lightweight and potential low cost of the active cathode material, the Metal-air system is a promising candidate for inexpensive, high energy density batteries. Recently, it has been shown that Na-air batteries, despite their lower energy density (1100 Wh kg^{-1} considering NaO_2 as discharge product) compared to the Li-air batteries (3450 Wh kg^{-1}), can achieve higher round trip efficiencies due to lower overpotentials and better rechargeability.[1, 2] To achieve such high capacity in a Na-air battery, it is crucial to optimize the nucleation/growth mechanism of NaO_2 during discharge. Several groups have demonstrated that NaO_2 forms via a one-electron reduction of O_2 followed by a solution-mediated precipitation of large, micrometer-sized cubes on the electrode surface.[3, 4-6] This is essential for achieving high capacity, as the low conductivity of NaO_2 would not support the electrochemical growth of large NaO_2 particles and would rather result in the formation of an insulating film that would block the electrode, ultimately leading to premature cell death.[7, 8]

However, despite many reports claiming a solution-mediated mechanism, the precise details of nucleation and growth of NaO_2 on carbon electrodes and the influential parameters are yet to be clarified. Experimentally, it has been shown that the conditions of discharge, such as the positive carbon electrode[9], the electrolyte solvent[5, 10] or even cycling conditions such as time and rate,[2, 6, 8, 11] have a drastic impact on the performance of Na-air battery.

Interestingly, in comparison to the Li-air system, where several electrode materials[12] and surface treatment methods have been explored,[13, 14] the investigation of electrode materials other than carbon[15, 16, 17] for the Na-air system is so far very limited.[18, 19]

We thus decided to embark into a comprehensive study, exploring and isolating the electrochemical and chemical processes governing the formation of NaO_2 in a Na-air battery. This work describes in details the effect of the positive host electrode, either carbon (C) or metallic gold (Au), and the relevant surface properties governing the discharge mechanism. The investigation of the electrochemical oxygen redox and the subsequent chemical growth mechanism of NaO_2 on C and

Au electrodes reveal the impact of the electrode surface on both processes. We demonstrate a strong surface dependence of the chemical growth and that its optimization is crucial to achieve high capacities and good performance in a Na-air battery.

2. Results and Discussion

2.1 Oxygen redox on carbon and gold surfaces

To explore the oxygen redox kinetics on gold (Au) and glassy carbon (GC) surfaces in diglyme (DGME) based electrolytes, cyclic voltammograms (CV) for the reduction and oxidation of oxygen were recorded under dry conditions (< 20 ppm H_2O). The CVs in presence of TBA^+ cations show the characteristic shape of a fast and quasi-reversible one-electron reduction of oxygen on both surfaces (**Figure 1 a**). We also find no specific effect of the electrode material on the kinetics of the redox process, indicating that the reduction of O_2 is relatively independent of the electrode surface, i.e. proceeding through outer-sphere electron transfer as proposed by Genorio *et al*.[20] However, the presence of Na^+-cations leads to a shift of the redox potential towards higher voltages (Figure 1 b). Recently we established that this shift can be explained by the stabilization of the O_2^- intermediate by Na^+.[5] Nevertheless, we observe very little effect of the electrode on the oxygen redox behavior in the presence of Na^+ when changing from GC to Au, further suggesting minor interactions between O_2 and the electrode during the ion-coupled reduction.

Several groups have demonstrated that the electrochemical reduction of O_2 is most likely followed by a chemical solution-mediated precipitation of NaO_2 leading to the formation of large NaO_2 cubes on the carbon electrode surface.[3, 4] This solution-mediated growth is explained by the small, but notable solubility of the NaO_2 species in glyme ethers DGME (approx. 10^{-4} mol L^{-1}).[4, 5] To examine if the kinetics of the delicate equilibrium between $NaO_{2(sol)}$ and $NaO_{2(surf)}$, is influenced by the nature of the electrode surfaces, rotating ring-disk electrode (RRDE) experiments were performed (Figure 1 c and d). The relative concentration of soluble O_2^- (Na^+-O_2^-) after the chemical reduction of O_2 is quantified by the oxidation current detected on the ring of the rotating electrode. For both surfaces, similar currents resulting from the oxidation of soluble O_2^- species were found,

implying that the use of an Au electrode would allow for a solution-mediated precipitation mechanism, similar to that occurring at carbon surfaces.

2.2 Impedance evolution of the electrode during discharge

To further explore the chemical precipitation (nucleation and growth) of NaO_2 on Au and C electrode surfaces, planar GC and Au electrodes were discharged in a NaOTf (0.5 M) containing DGME electrolyte. In addition, electrochemical impedance spectroscopy (EIS) measurements were performed during discharge to monitor the accumulation of insulating species like NaO_2 on the surface of the electrode, as reported by others.[21] The planar electrodes were discharged by galvanostatic intermittent titration technique (GITT) and EIS measurements performed during the OCV period until the cell potential dropped below 1.8 V. Intriguing differences were observed when comparing the discharges on planar GC and Au electrodes (**Figure 2**). Notably, the capacities obtained using the Au electrode were less than half that found for the GC electrode. This is surprising when one considers the similar oxygen redox and NaO_2 solubility found by RRDE (Figure 1). However, deeper insight into the origins of this effect can be obtained from the EIS data (Figure 2 b and d). The Au-electrode shows a much larger and faster increase in impedance at very early stages of discharge compared to GC (**Figure S1**). The impedance spectra were treated using the methodology described by Knudsen et al. which neglects the porosity of the electrode; this methodology is well adapted for the planar electrodes used in the present study (Schematic S1).[21] The premature death of cells correlates with an increase of the charge transfer resistance at the working electrode (R_{CT}) (Figure S1). This observation is in good agreement with previous reports on carbon electrodes and was ascribed to the coverage of the working electrode by insulating products, such as NaO_2, which prevent further O_2 redox.[21, 22] Hence, the origin for the large discrepancy observed for cell performances in Figure 2 most likely results from a different nucleation/growth process for NaO_2 on the surface of Au compared to GC, which will be discussed in the following section.

2.3 Discharge of Na-air cells using Carbon and Gold electrodes

Although CV studies and planar discharges are essential to understand the oxygen reduction mechanism and the formation of NaO_2 on various surfaces, caution must be exercised in correlating these observations to the behavior of Na-air batteries. In order to determine if these effects influence the battery under real conditions, porous carbon electrodes, namely a gas diffusion layer (GDL) typically used for experiments on Na-air systems, were employed as positive electrodes.[1, 5] Further, GDL electrodes were coated with gold (Au-GDL) by plasma sputtering (approx. 20 - 30 nm in thickness) onto the GDL support so as to avoid any alteration of the microstructure and porosity of the cathode. Comparable morphologies and electrochemical oxygen redox behaviors for untreated GDL and Au-coated GDL were confirmed by SEM and CV measurements (**Figure S4**).

The discharge profile obtained with GDL electrodes is similar to what has been previously reported,[1, 5] i.e. a single plateau at ~ 2.1 V with a discharge capacity of around 4 mAh $cm^{-2}_{(geom)}$ associated with the formation of crystalline NaO_2 cubes on the surface of the electrode (**Figure 3** a, black line). The formation of crystalline NaO_2 was verified by monitoring the O_2 pressure change relative to the charge passed, yielding a ratio of 1 e^- / O_2 (Figure 3 b), and confirmed by XRD (Figure 3 c). Using Au-GDL electrodes, the voltage rapidly decays from an initial discharge plateau at ~ 2.1 V resulting in a limited capacity of ~ 1 mAh cm^{-2} (a, yellow line). The oxygen pressure decrease monitored during the discharge as well as XRD analysis confirmed the formation of crystalline NaO_2 as the main discharge product (b and c, yellow line). The columbic efficiency was found to be comparable when using GDL or Au-GDL electrodes; this was further verified by using shallow cycling with a capacity of 0.5 mAh cm^{-2} (**Figure S5**). The reproducibility of the obtained results was satisfactory for both Au-GDL, (1.3 ± 0.4 mAh cm^{-2}) and for GDL electrodes (4.3 ± 0.2 mAh cm^{-2}), details in **Figure S6**.

2.4 Morphology of the discharge products

In summary, electrochemical analysis discussed above indicates that the use of Au electrodes results in a lower discharge capacity for the Na-air battery due to the elevated accumulation of insulating NaO_2 at the electrode surface. To confirm this, we studied the morphology of the

discharge product formed on the surface of GDL and Au-GDL electrodes by SEM and STEM-EDX mapping (**Figure 4**). For the GDL electrode, large cubes of NaO_2 were found (Figure 4 a, b, c). In contrary, the Au-coated fibers were found to be nearly fully covered by ~ 3-5 μm large flake-like structures (Figure 4 d, e, f) which, in light of their thin structure, host less NaO_2 than large cubes formed on GDL. Due to the very low conductivity of NaO_2,[4, 7] we propose that the vast coverage by flakes subsequently blocks O_2 reduction at the electrode surface, explaining the obtained differences in Figure 3 and ultimately leading to premature cell death compared to cells in which NaO_2 cubes are formed. As the basic oxygen reduction is independent on the surface chemistry, it can be hypothesized that the origin for this effect is due to differences in the nucleation/growth mechanism of NaO_2 at GC and Au, which we explore next.

2.5 Evolution of cubes and flakes

In light of these surprising results, the morphological evolution of the discharge product within Na-air cells containing GDL and Au-GDL cathodes was explored at 0.3 mAh $cm^{-2}$and 1 mAh cm^{-2} during discharge (**Figure 5**). Considering first the untreated GDL, NaO_2 forms discreet nuclei at low capacities (Figure 5 b). The minimal contact with the electrode and thus low coverage of the electrode surface with passivating oxide is observed at even higher capacities (Figure 5 c). This allows for further reducing oxygen, as well as allowing further nucleation and growth of NaO_2, consistent with the continuous discharge that eventually leads to the growth of micron-sized cubes yielding capacities of around 4 mAh cm^{-2}. Interestingly the size distribution of the cubes is inhomogeneous (**Figure S7** a) throughout discharge. Nuclei and small cubes of various sizes were found on the surface of the electrode, indicating that the nucleation is not a single event occurring at the beginning of discharge, but rather a progressive nucleation process. Since the nucleation of NaO_2 on GDL fibers appears only at certain distinct spots on the carbon fiber, we further believe that the nucleation process of NaO_2 from solution follows a heterogeneous nucleation, initiated by high-energy surface sites on the GDL fiber. Such nucleation sites could be surface defects or fluoride/nitrogen groups found on the GDL fiber surface (**Figure S8**).

Turning to the Au-GDL electrodes, the product formed after discharge to 0.3 mAh cm^{-2} covers a much higher electrode area than the cubes found on the surface of bare GDL at the same stage (Figure 5 e). Indeed, a dense network of ~ 2 μm (in length) flakes was observed, covering a vast surface of the electrode at 1 mAh cm^{-2}. The formation of thin flakes, which display a low NaO_2 volume per electrode area, but a large contact area with the electrode, would explain the minor capacity per cm^2 obtained with this morphology. Therefore, we ascribe the rapid increase in resistance during discharge found in Figure 3, to the higher surface interaction of the flakes with Au-coated surface, covering more electrode surface than the cubes. This finding, combined with the impedance studies performed in this work and by other groups, [21, 22] bolsters the contention that the cell death is actually caused by blockage of the electrode through the formation of insulating metal-oxide species, preventing any further O_2 reduction.

2.6 Nucleation kinetics of NaO_2

To rationalize such differences, the parameters influencing the chemical formation of NaO_2 on the electrode surface must be recalled. First, the electrochemical reduction of O_2 takes place, forming O_2^- which reacts with Na^+ in solution to form the solvated $NaO_{2(solv)}$ complexes. Upon saturation of the electrolyte, the complexes eventually desolvate before to nucleate and grow on the surface of the electrode. The rate for the chemical nucleation of NaO_2 can therefore be described by:

$$r_{NaO_2} = \frac{K_B T}{h} exp\left(-\frac{\Delta G}{K_B T}\right) \quad (1)$$

with K_B being the Boltzman constant, h the Plank constant, T the temperature and ΔG the activation free energy. [18] In the case of a solution precipitation mechanism, the nucleation of NaO_2 (ΔG_{NaO2}) depends on the solvent and the electrode surface energy, as describe in equation 2;

$$\Delta G_{NaO_2} = \left(G_{E-NaO_2}\right) - \left(G_{S*} + G_{NaO_{2(solv)}}\right) \quad (2)$$

where $G_{(E\text{-}NaO2)}$ represents the energy of NaO_2 absorbed to the electrode surface, G_{S*} the energy of a surface site and $G_{NaO2(solv)}$ the energy of solvated NaO_2. In our case, $G_{NaO2(solv)}$ can be taken as a constant since the same electrolyte is used throughout the study. Therefore, we postulate that the

major influence on the rate of nucleation of NaO_2 is nested in the difference in energy existing for the surface stabilization and the affinity of the surface towards oxygen.

The values for the specific surface energy of C and Au as well as their O_2 affinities, assuming that the binding energies of different O species (O_2/O_2^-) towards a surface scale equally, are displayed in **Table S1**. It is immediately obvious that Au interactions with NaO_2 are favored by decreasing ΔG_{NaO2} through: i) lowering the Au surface energy when in contact with NaO_2 and ii) a stronger interaction of O_2^- and the Au surface.

2.7 The interplay between NaO_2 and the electrode surface

Within this context, we further explored the interaction of NaO_2 with the electrode surface. For this purpose, XPS spectra of the O (1s) and Au (4f) peaks were collected at an Au-GDL electrode before and after discharge (**Figure 6**). When looking at the O (1s) spectra, the evolution of NaO_2 on the surface of the electrode upon discharge can be observed by the growth of the peak at 532.2 eV, ascribed to NaO_2 (Figure 6 b).[23, 24] When turning to the Au (4f) spectra, the results further confirm the existing interaction of O_2^- with Au, ultimately resulting in the oxidation of the pristine $Au^{(0)}$ surface (Figure 6 d). These findings demonstrate the above-described energetically favored interaction of Au with O_2^-. The Au-O interaction can be either covalent or be resulting from O_2^- shared between Au and Na^+ on the surface of the electrode. Subsequently, these Au-O sites can then act as preferential nucleation points for NaO_2 and would explain the fast and altered growth of NaO_2, leading to flakes-like particles when using Au-electrodes.

The inherent stronger chemical interaction between the O_2^- and the Au surface and the resulting effect on the growth of NaO_2 was further demonstrated by chemically precipitating KO_2 from solution onto GDL and Au-coated GDL substrates. For that, GDL and Au-GDL electrodes were imbedded into KO_2-saturated dry DGME solutions and the growth of KO_2 on these substrates was subsequently analyzed by SEM (**Figure S9**). Even though the final product shows a different morphology from the electrochemically formed NaO_2, vastly different growth patterns were observed depending on the electrode surface. At the untreated GDL, small distinctive nucleation

clusters formed, leading to a 3D growth towards solution with minimal contact between the electrode surface and KO_2 (Figure S9 a, b), whereas on Au-GDL the interaction between KO_2 and the surface is favored, promoting formation of a 2D island-like growth across the electrode surface (Figure S9 c, d).

These interesting results highlight that the oxygen reduction and the mechanism for the electrochemical formation of $NaO_{2(solv)}$ are indeed independent of the surface of the electrode. However, we could demonstrate that the subsequent chemical step, the crystallization of NaO_2, is highly affected by the electrode surface. On carbon electrodes the precipitation of NaO_2 results in large crystalline cubes via heterogeneous, persistent and distinct nucleation and growth of NaO_2 on surface defects. On the other hand, in the case of Au electrodes, high surface energy and elevated superoxide affinity result in preferential nucleation of NaO_2 at the Au surface. The resulting 2D-like growth with an altered morphology of NaO_2 ultimately limits the capacity of the Na-air cell (Scheme 1).

This finding makes the interface between NaO_2 and the electrode a critical parameter to control for achieving highly efficient Na-O_2 batteries. Arising from this study, one can wonder if through the choice of appropriate surface it would be possible to further reduce the surface interaction of NaO_2 with the cathode to enhance the capacity, exhibit a greater stability and a smaller contact area with the electrode at the same time.

3. Conclusion

In this paper, we demonstrate the impact of the positive electrode on the electrochemical and chemical reaction steps in a Na-air battery. Firstly we found that the electrode surface has a minor effect on the electrochemical O_2 reduction in the presence of Na^+ or TBA^+ cations in glyme-ethers. However, the subsequent chemical growth of NaO_2 during discharge is highly dependent on the surface properties of the electrode, namely i) the surface energy and ii) the superoxide affinity, where both factors ultimately determine the capacity of a Na-air battery. For Au electrodes, the high

surface energy and large superoxide affinity lead to elevated interaction between Na-O_2 and the electrode surface. This interaction results in facilitated nucleation, altered growth and a premature coverage of the electrode with insulating discharge product. We showed that a low contact area between the insulating discharge product and the electrode surface has to be achieved in order to reach large capacities in Na-air-batteries.

These results further stress the significant differences existing between the Li-air and the Na-air systems, in particular the different reactivity of NaO_2, LiO_2 intermediate and Li_2O_2 with the electrode surface. For the Li-air battery the electrode seems to have a minor influence on the growth of toroidal Li_2O_2 and inversely, for the Na-air system, the surface-dependent formation of NaO_2 requires new approaches to guarantee high performance and long term stability of the battery, hence a wide field of opportunities to properly prepare suitable electrode surfaces.

4. Experimental Section

Chemicals and Materials: Diethylene glycol dimethylether (DGME, 99.5%), Sodium trifluoromethanesulfonate (NaOTf, 98 %) and Tetrabutylammonium trifluoromethanesulfonate (TBA-OTf, 99 %99 %) were purchased from Sigma Aldrich. The binder free gas diffusion layer (GDL, Freudenberg H2315), here used as electrode, was obtained from Quintech. Prior to use the GDL was dried under vacuum at 260°C for 24 hours.

Solvents were dried over freshly activated molecular sieves (4 Å) for several days. Sodium salts were dried under vacuum at 80°C for 12 -24 hours. The electrolyte solutions (0.5 M) were prepared in an argon-filled glove box (0.1 ppm O_2/0.1 ppm H_2O). The water content of the electrolyte solutions was analyzed by Karl Fischer titration and was found to be below 20 ppm.

Au-GDL electrode preparation: GDL electrodes were coated with gold via plasma sputtering using a Mini Plasma Sputtering Coater (MTI). Sputtering conditions; time (60 s), current (18 mA), and Argon pressure (8 Pa) were optimized to a thickness of 20 nm, by calibrating the sputtered gold thickness using a Quartz Crystal Micro Balance.

Cyclic voltammetry (CV) and rotating disc electrode (RRDE) experiments: Electrochemical measurements were performed inside an argon/oxygen-filled dry box (< 0.5 ppm H_2O) at room temperature using IR-correction. Solvents were redistilled, prior to use. Rotating Ring Disc Electrode (RRDE) measurements were performed using a Pine AFMSRCE setup in combination with a Bio-Logic VMP3 potentiostat. Either a fixed rotating ring/disk electrode containing a Gold (Au) disc (0.5 mm) and Au ring (Pine instruments) or a GC disc (0.5 mm) or Pt ring (Pine instruments) were used as a working electrode. The working electrodes were polished with aluminum paste (0.05 µm). The electrodes were subsequently rinsed with ethanol and deionized water, sonicated and dried at elevated temperature under vacuum. A Platinum (Pt, 99.9 %) wire was used as a counter electrode. An Ag^+/AgCl reference electrode was used (Ag wire in a 0.01 M $AgNO_3$ / 1 M TBAP ACN solution, Biologic) in all the electrochemical measurements. The solutions were saturated with oxygen by bubbling ultra-pure O_2 gas (Linde, < 0.5 ppm H_2O, < 0.1 ppm CO_2), dried by means of multiple moisture traps. The water content was checked by Karl Fischer titration to be < 20ppm after each measurement. For sake of clarity, all values were then rescaled versus Na^+/Na. All measurements were obtained at room temperature in a three necked round bottom flask. The disc potential was scanned at a speed of 20 mV s^{-1}. The Ring potential was kept at 0 V *vs*. Ag^+/AgCl. During RRDE measurements a rotation speed of 1000 rpm was applied to the working electrode. For CV measurements the disc was scanned at 100 mV s^{-1}.

Cell assembly and electrochemical measurements: Na-O_2 cells were built from a modified Swagelok setup. The Swagelok cell was connected to a pressure monitor in order to analyze pressure changes during cycling. The cell was vacuum dried under elevated temperature and transferred into a glove box (0.1 ppm H_2O, 0.1 ppm O_2). The anode was made from metallic sodium (Sigma Aldrich), cut into a 0.5 cm^2 disc. Dried electrolyte solution (0.5 M NaOTf in DGME) was imbibed on two Whatman glass fiber filters (QM-A grade) (dried under vacuum at 260°C, 24 hours), about 0.3 ml. A piece of GDL (1.13 cm^2 of surface area, 210 um in thickness and a weight of 10 mg) was used as cathode and held by an aluminum current collector containing holes for gas exchange. The assembled cells were transferred from the glove box to a filling station and after a first evacuating step, the cells were pressurized with dry, ultrapure O_2 to 1.3 bar. In order to guarantee stable temperature conditions, the cells were mounted inside of a temperature-controlled incubator (25.0 ± 0.1 °C). The electrochemical measurements were performed under temperature-controlled conditions (25.0 ^oC) after resting for 4 hours at the open circuit voltage and using a Bio-Logic VMP3 potentiostat. Pressure analysis decay analysis and e^-/O_2 ratios were calculated like described elsewhere.[25]

Electrochemical impedance spectroscopy (EIS) measurements: EIS was performed using a Biologic SP300, a GC or Au planar working electrode (3mm) and metallic sodium as a counter and reference electrode in a three necked round bottom flask. Spectra were recorded at OCV after 1 min intervals of discharge and a 2 min relaxation period at OCV, using an ac amplitude of 10 mV, while the frequency was varied from 3 MHz to 30 mHz with 5 points per decade and 10 cycles per frequency. Typically 60 − 130 EIS spectra were obtained for one discharge.

Scanning Electron Microscopy (SEM): Samples were washed with dried DME prior to SEM imaging. All samples were transferred by means of a hermetic transfer chamber to avoid exposure to ambient air. SEM images were acquired on a FEI Magellan 400 XHR microscope equipped with

FEG source. An Oxford Instruments Energy Dispersive X-ray (EDX) spectroscopy system mounted on a Zeiss Merlin SEM was used for chemical composition analysis. All SEM data were acquired using accelerating voltage of 5 kV.

Scanning Transmission Electron Microscopy - EDX (STEM-EDX) analysis: Samples for TEM were prepared in an Ar-filled glovebox. The electrodes were scored with a scalpel and the loose fragments of fiber were attached to a blank Cu TEM grid. Special Gatan vacuum transfer holder was used for analysis. Scanning TEM (STEM) images and the STEM-EDX data were acquired on an FEI Osiris electron microscope operated at 200 kV, which equipped with a Super-X EDX detector.

X-Ray diffraction (XRD): Samples were washed with dried DME prior to XRD analysis. A Bruker D8 Advance diffractometer with a Cu-Kα radiation source (λ1 =1.5405Å, λ2 = 1.5443Å) and a Lynxeye XE detector was used to collect the XRD patterns. The XRD patterns were recorded for 30 min in the 2θ range of 20-65 °. A special airtight cell with a beryllium window was used to guarantee no ambient air contamination during XRD measurements.

X-ray Photoelectron Spectroscopy: XPS experiments were performed in a SPECS Sage HR 100 spectrometer with a non-monochromatic X-ray source (Aluminum Kα line of 1486.6 eV energy and 300 W). The samples were placed perpendicular to the analyzer axis and calibrated using the $3d_{5/2}$ line of Ag with a full width at half maximum (FWHM) of 1.1 eV.

The selected resolution for the spectra was 10 eV of Pass Energy and 0.15 eV per step. All Measurements were made in an ultra-high vacuum (UHV) chamber at a pressure around $5 \cdot 10^{-8}$ mbar. An electron flood gun was used to compensate for charging during XPS data acquisition.

In the fittings asymmetric Gaussian-Lorentzian functions were used (after a Shirley background correction) where the FWHM of all the peaks were constrained while the peak positions and areas were set free.

Supporting Information
Supporting Information is available from the Wiley Online Library or from the author.

Acknowledgements

L.Lutz thanks ALISTORE-ERI for his PhD grant.

References

[1] P. Hartmann, C. L. Bender, M. Vracar, A. K. Duerr, A. Garsuch, J. Janek, P. Adelhelm, *Nat. Materials*, **2013**, *12*, 228.
[2] P. Adelhelm, P. Hartmann, C. L. Bender, M. Busche, C. Eufinger, J. Janek, *Beilstein J. Nanotechnol*., **2015**, *6*, 1016.
[3] a) P. Hartmann, C. L. Bender, J. Sann, A. K. Duerr, M. Jansen, J. Janek, P. Adelhelm, *Phys. Chem. Chem. Phys*., **2013**, *15*, 11661; b) B. D. McCloskey, J. M. Garcia, A. C. Luntz, *J. Phys. Chem. Lett.*, **2014**, *5*, 1230.
[4] P. Hartmann, M. Heinemann, C. L. Bender, K. Graf, R.-P. Baumann, P. Adelhelm, C. Heiliger, J. Janek, *J. Phys. Chem. C*., **2015**, *119*, 22778.
[5] L. Lutz, W. Yin, A. Grimaud, D. Alves Dalla Corte, M. Tang, L. Johnson, E. Azaceta, V. Sarou-Kanian, A. J. Naylor, S. Hamad, J. A. Anta, E. Salager, R. Tena-Zaera, P. G. Bruce, J. M. Tarascon, *J. Phys. Chem. C*., **2016**, *120*, 20068.
[6] D. Schroder, C. L. Bender, M. Osenberg, A. Hilger, I. Manke, J. Janek, *Sci. Rep.*, **2016**, *6*, 24288.
[7] S. Yang, D. J. Siegel, *Chem. Mater*., **2015**, *27*, 3852.
[8] J. Kim, H. Park, B. Lee, W. M. Seong, H. D. Lim, Y. Bae, H. Kim, W. K. Kim, K. H. Ryu, K. Kang, *Nat. Commun.*, **2016**, *7*, 10670.

[9] C. L. Bender, P. Hartmann, M. Vracar, P. Adelhelm, J. Janek, *Adv. Energy Mater*, **2014**, *4*, 1301863
[10] E. Azaceta, L. Lutz, A. Grimaud, J. M. Vicent-Luna, S. Hamad, L. Yate, G. Cabanero, H. J. Grande, J. A. Anta, J. M. Tarascon, R. Tena-Zaera, *ChemSusChem*, **2017**, *10*, 1616.
[11] S. Y. Sayed, K. P. Yao, D. G. Kwabi, T. P. Batcho, C. V. Amanchukwu, S. Feng, C. V. Thompson, Y. Shao-Horn, *Chem Commun*, **2016**, *52*, 9691.
[12] Z. Peng, S. A. Freunberger, Y. Chen, P. G. Bruce, *Science*, **2012**, *337*, 563.
[13] M. M. Ottakam Thotiyl, S. A. Freunberger, Z. Peng, Y. Chen, Z. Liu, P. G. Bruce, *Nat. Mater.*, **2013**, *12*, 1050.
[14] S. H. Oh, R. Black, E. Pomerantseva, J. H. Lee, L. F. Nazar, *Nat. Chem*, **2012**, *4*, 1004.
[15] H. Yadegari, M. N. Banis, B. Xiao, Q. Sun, X. Li, A. Lushington, B. Wang, R. Li, T.-K. Sham, X. Cui, X. Sun, *Chem. Mater*., **2015**, *27*, 3040.
[16] Q. Sun, H. Yadegari, M. N. Banis, J. Liu, B. Xiao, B. Wang, S. Lawes, X. Li, R. Li, X. Sun, *Nano Energy*, **2015**, 1*2*, 698.
[17] H. Yadegari, Y. Li, M. N. Banis, X. Li, B. Wang, Q. Sun, R. Li, T.-K. Sham, X. Cui, X. Sun, *Energy Environ. Sci*., **2014**, *7*, 3747.
[18] D. Krishnamurthy, H. A. Hansen, V. Viswanathan, *ACS Energy Letters*, **2016,** *1*, 162.
[19] V. Viswanathan, H. A. Hansen, J. Rossmeisl, J. K. Norskov, *J. Phys. Chem. Lett.*, **2012**, *3*, 2948.
[20] B. Genorio, J. Staszak-Jirkovský, R. S. Assary, J. G. Connell, D. Strmcnik, C. E. Diesendruck, P. P. Lopes, V. R. Stamenkovic, J. S. Moore, L. A. Curtiss, N. M. Markovic, The *J. Phys. Chem.* C., **2016**, *120*, 15909.
[21] K. B. Knudsen, J. E. Nichols, T. Vegge, A. C. Luntz, B. D. McCloskey, J. Hjelm, The *J. Phys. Chem.* C., **2016**, *120*, 10799.
[22] I. Landa-Medrano, J. T. Frith, I. Ruiz de Larramendi, I. Lozano, N. Ortiz-Vitoriano, N. Garcia-Araez, T. Rojo, *J. Power Sources*, **2017**, *345*, 237.
[23] NIST X-ray Photoelectron Spectroscopy Database (NIST Standard Reference Database 20); online Version 4.1.
[24] J. F. Moulder, W. F. Stickle, P. E. Sobol, K. D. Bomben, *Handbook of X ray Photoelectron Spectroscopy.*, Norwalk **1995**.
[25] P. Hartmann, D. Grubl, H. Sommer, J. Janek, W. G. Bessler, P. Adelhelm, *J. Phys. Chem. C.*, **2014**, *118*, 1461.

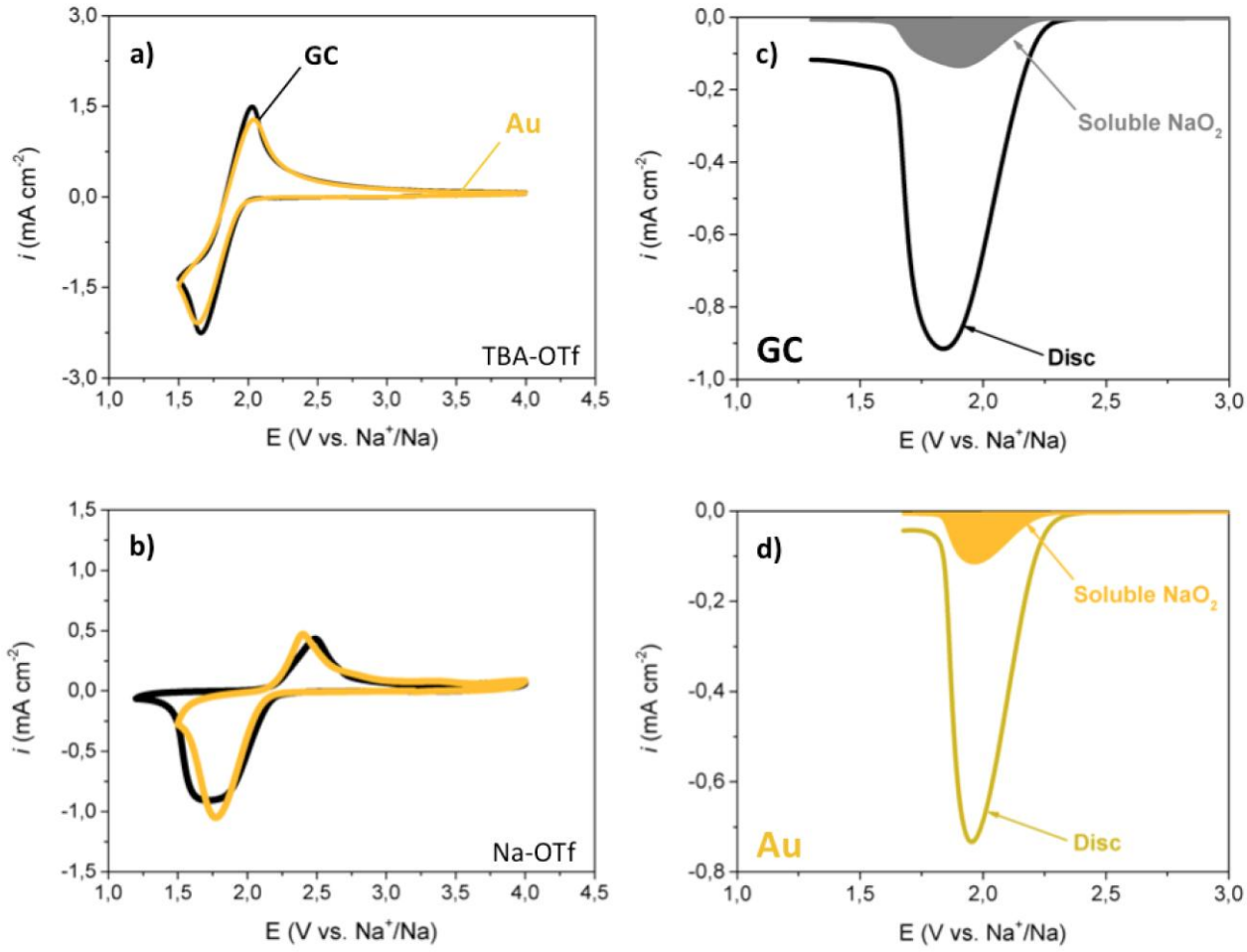

Figure 1: Cyclic voltammograms of oxygen reduction on GC (black) and Au (yellow) surfaces at 100 mV s^{-1} in DGME using 0.5 M TBAOTf (a) and 0.5 M NaOTf (b) as conductive salt. RRDE measurements performed using GC(disc) - Pt(ring) (c) and Au-Au (d) working electrodes in oxygen saturated DGME with 0.5 M NaOTf (H_2O < 20 ppm after measurement). The disk was scanned at a rate of 20 mV s^{-1} and an oxidation potential of 3 V Na^+/Na was applied to the ring at a rotation speed of 1000 rpm to detect soluble superoxide species.

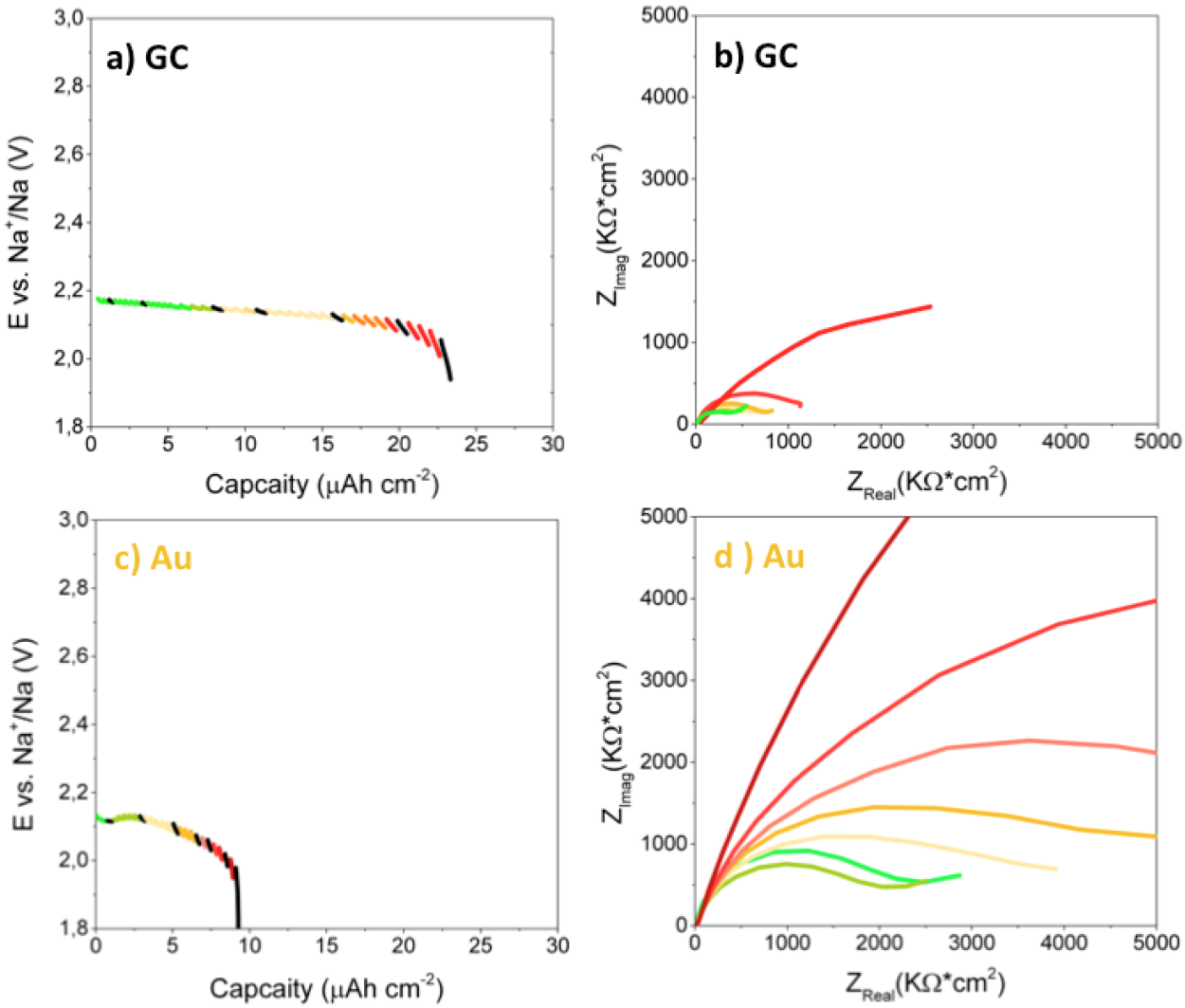

Figure 2: GITT discharges at 100 uA cm^{-2} in DGME with 0.5M NaOTf using a planar GC (a, b) or a planar Au electrode (c,d), and the according impedance evolution over time (green to red). Impedance spectra were recorded at OCV after 1 min intervals of discharge and a stabilization time at OCV of 2 min.

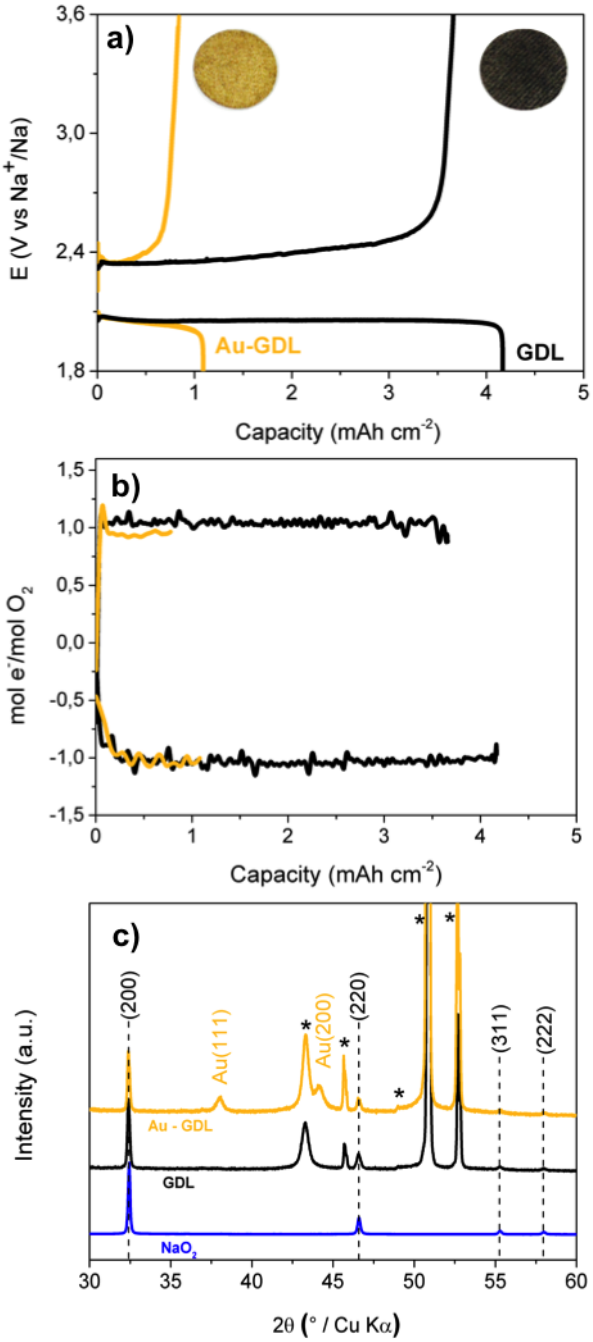

Figure 3: Discharge/charge profiles for GDL and Au-coated GDL cells using a 0.5 M NaOTf DGME electrolyte and a rate of 25 µA cm^{-2} (a). Inserts show images of the pristine (black) and Au-covered (gold) GDL electrodes. Pressure monitoring of O_2 pressure decrease and rise during discharge and recharge respectively (b). Both profiles show a ratio of 1 e^- per O_2. XRD patterns of the discharged GDL (black) and Au-GDL (yellow) electrodes indicate that the main product is NaO_2 (c). Black indices correspond to NaO_2 provided by Prof. M. Jansen (MPI-FKF, Stuttgart, Germany), yellow indices mark Au reflections and * peaks corresponds to the sample holder.

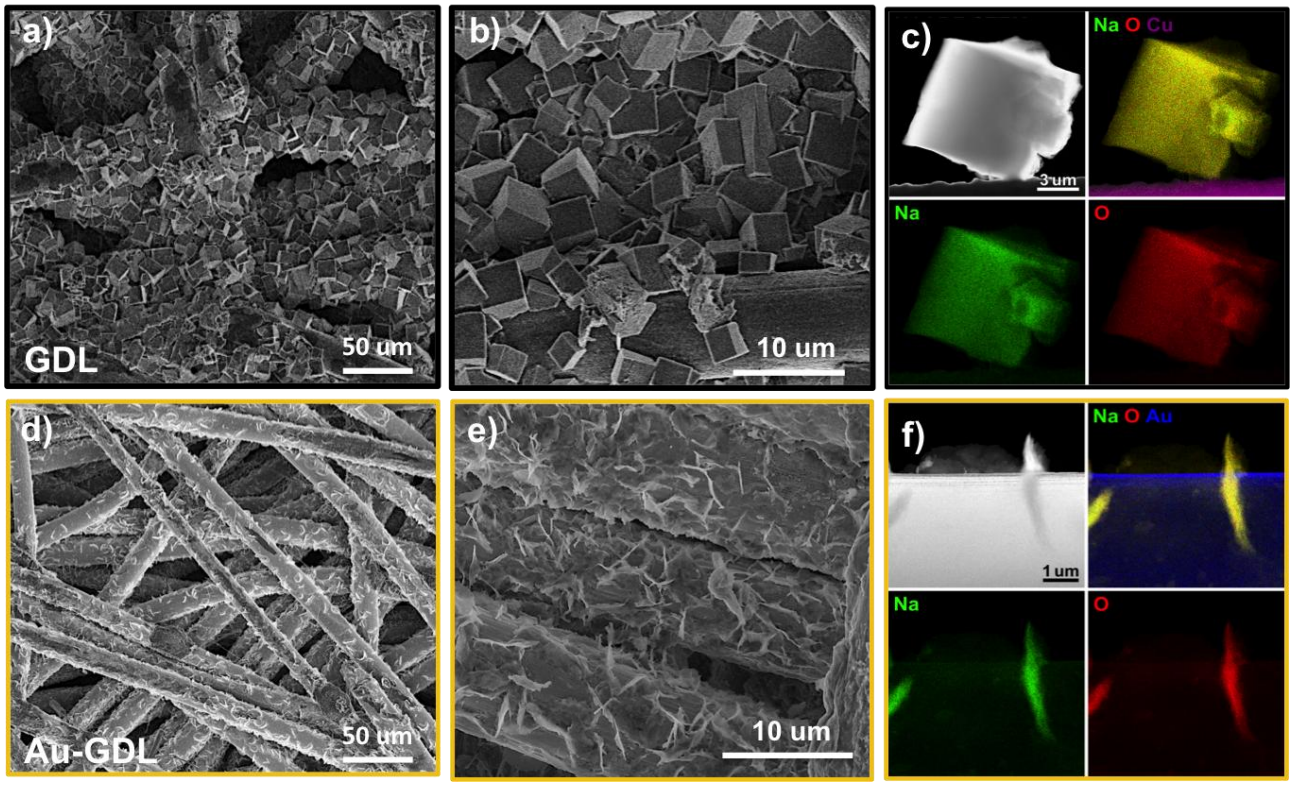

Figure 4: SEM and STEM-EDX data for fully discharged GDL (black) and Au-GDL (yellow) electrodes in DGME electrolyte. Low magnification of assembly of NaO_2 cubes covering GDL fibers (a) and zoom on interconnected cubes on a GDL fiber (b). Overview of Au-GDL fibers coated by NaO_2 flakes (d) and high magnification of 3-5 um long flakes on Au-GDL fibers (e). HAADF-STEM image together with the corresponding elemental maps for NaO_2 cubes in the GDL sample (c) and Na-O flakes on an Au-GDL fiber (f).

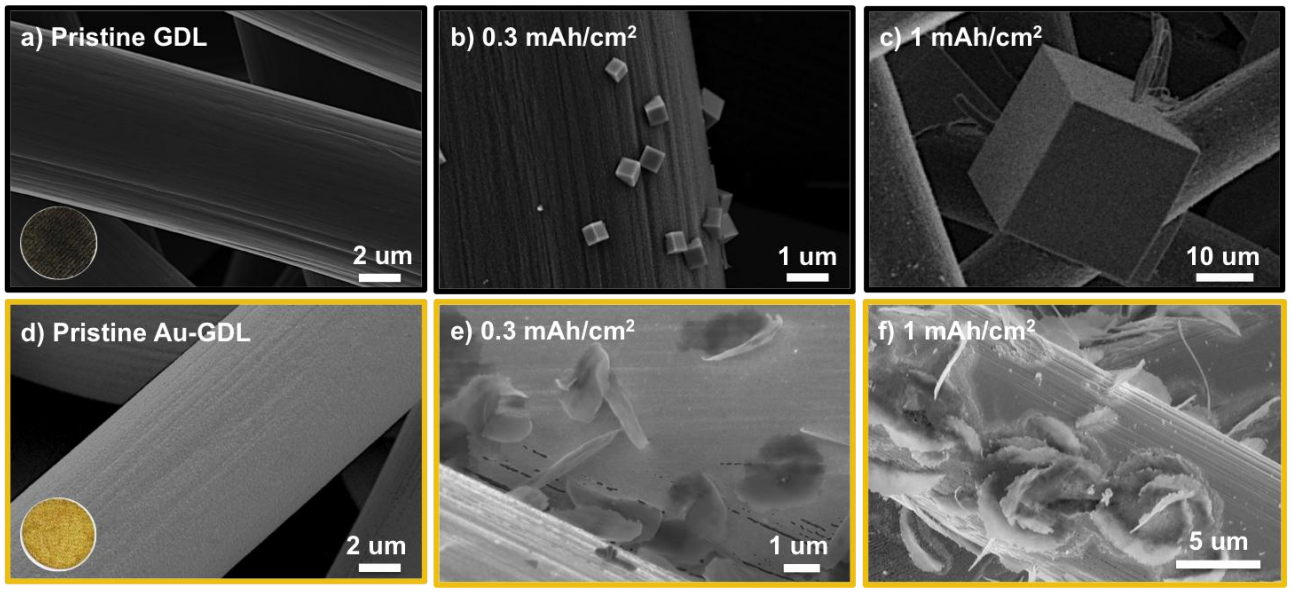

Figure 5: SEM images of GDL (black) and Au-GDL electrodes (yellow) at various stages of discharge showing the difference in nucleation and growth. Pristine (a)/(d), 0.3 mAh cm^{-2} (b)/(e) and 1 mAh cm^{-2} (c)/(f). Insert in (a), picture of a GDL electrode (1.1 cm^2). Insert in (d) picture of an Au-coated GDL electrode (1.1 cm^2).

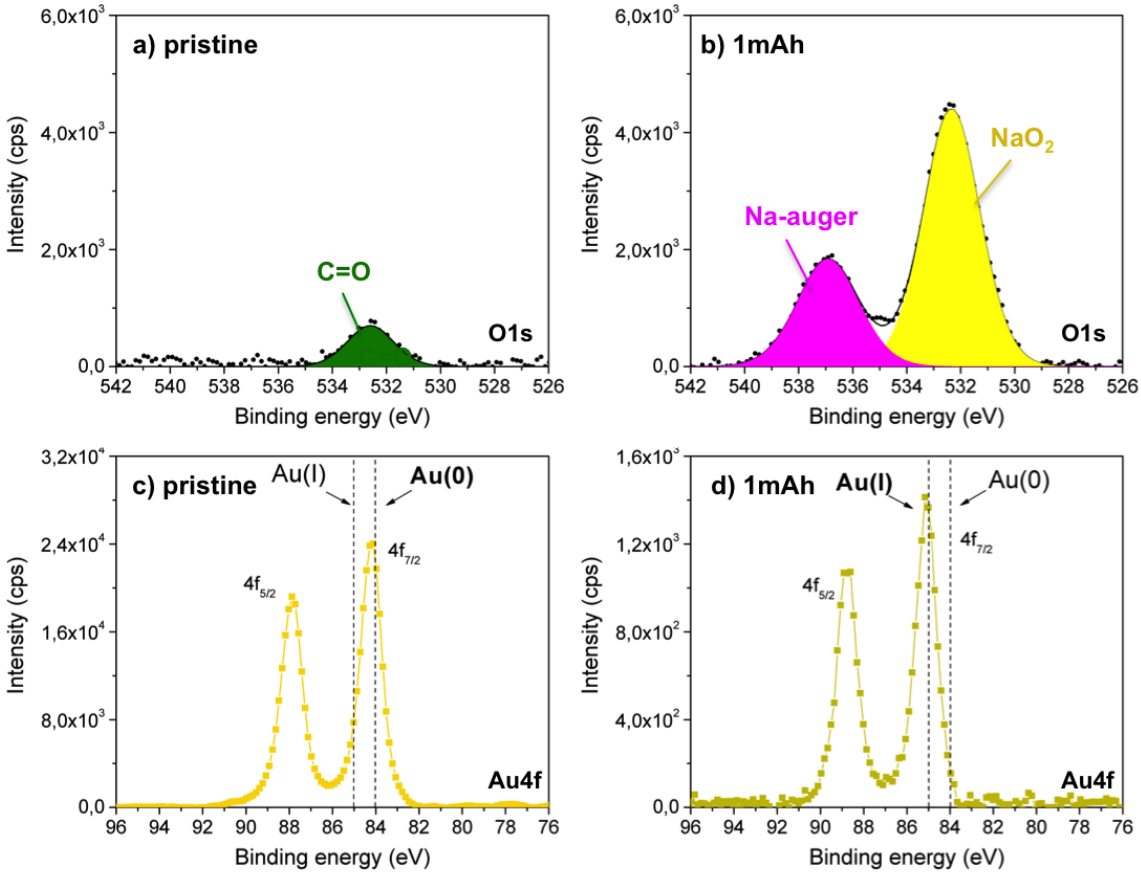

Figure 6: XPS analysis of the O 1s and Au 4f peak on a pristine Au-GDL surface (a, c) compared to a fully discharged Au-GDL electrode (b, d). The shift of the Au 4f peak towards lower energies is confirming the strong interaction (oxidation) between the Au-GDL surface and the NaO_2 (O_2^-) discharge product. [24]

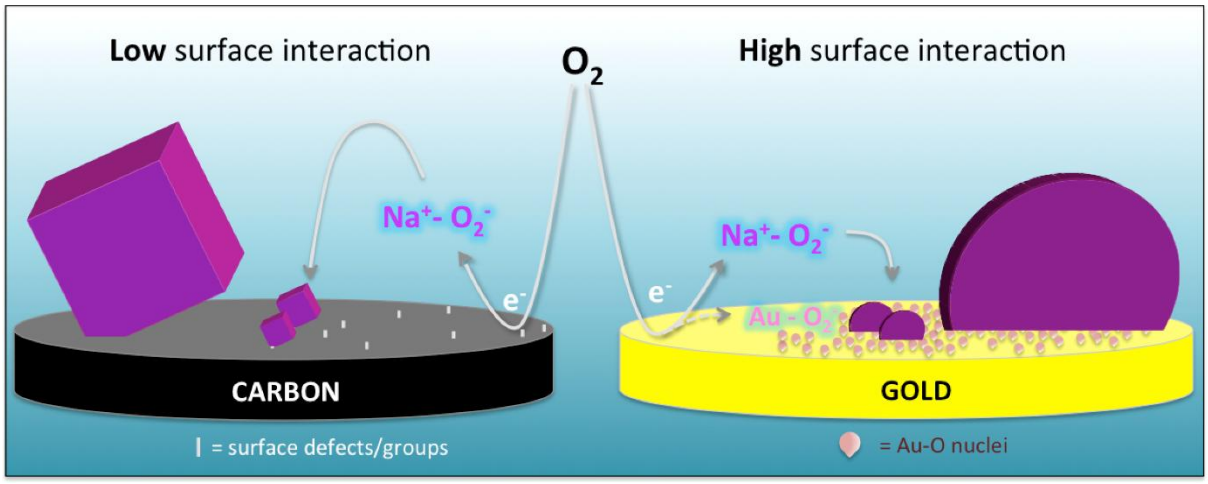

Scheme 1: Summary of NaO_2 crystallization pathways on carbon and gold surfaces.

ToC figure

In NaO_2 batteries, the chemical crystallization (growth) of NaO_2 is highly sensitive to the surface energy and O_2/O_2^- affinity of the electrode. On Gold, strong interaction with O_2^- leads to formation of small NaO_2 flakes, while on Carbon (low surface energy) large NaO_2 cubes are found. This has significant impact on the cell performance.

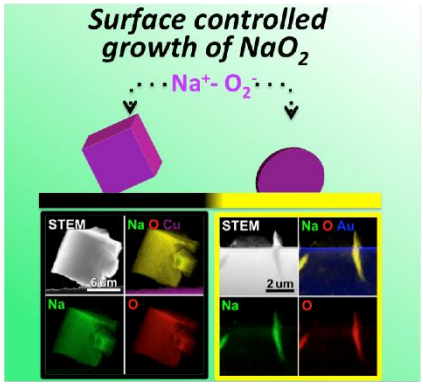

Keywords: Na-air battery, Na-O_2 battery, NaO_2 growth, oxygen redox, electrode surface

Title: The role of the electrode surface in Na-air batteries; insights in electro-chemical product formation and chemical growth of NaO_2.

Lukas Lutz, Daniel Alves Dalla Corte, Yuhui Chen, Dmitry Batuk, Lee R. Johnson, Artem Abakumov, Luis Yate, Eneko Azaceta, Peter G. Bruce, Jean-Marie Tarascon and Alexis Grimaud*

Supporting Information

Title: The role of the electrode surface in Na-air batteries; insights in electro-chemical product formation and chemical growth of NaO_2.

Lukas Lutz, Daniel Alves Dalla Corte, Yuhui Chen, Dmitry Batuk, Lee R. Johnson, Artem Abakumov, Luis Yate, Eneko Azaceta, Peter G. Bruce, Jean-Marie Tarascon and Alexis Grimaud*

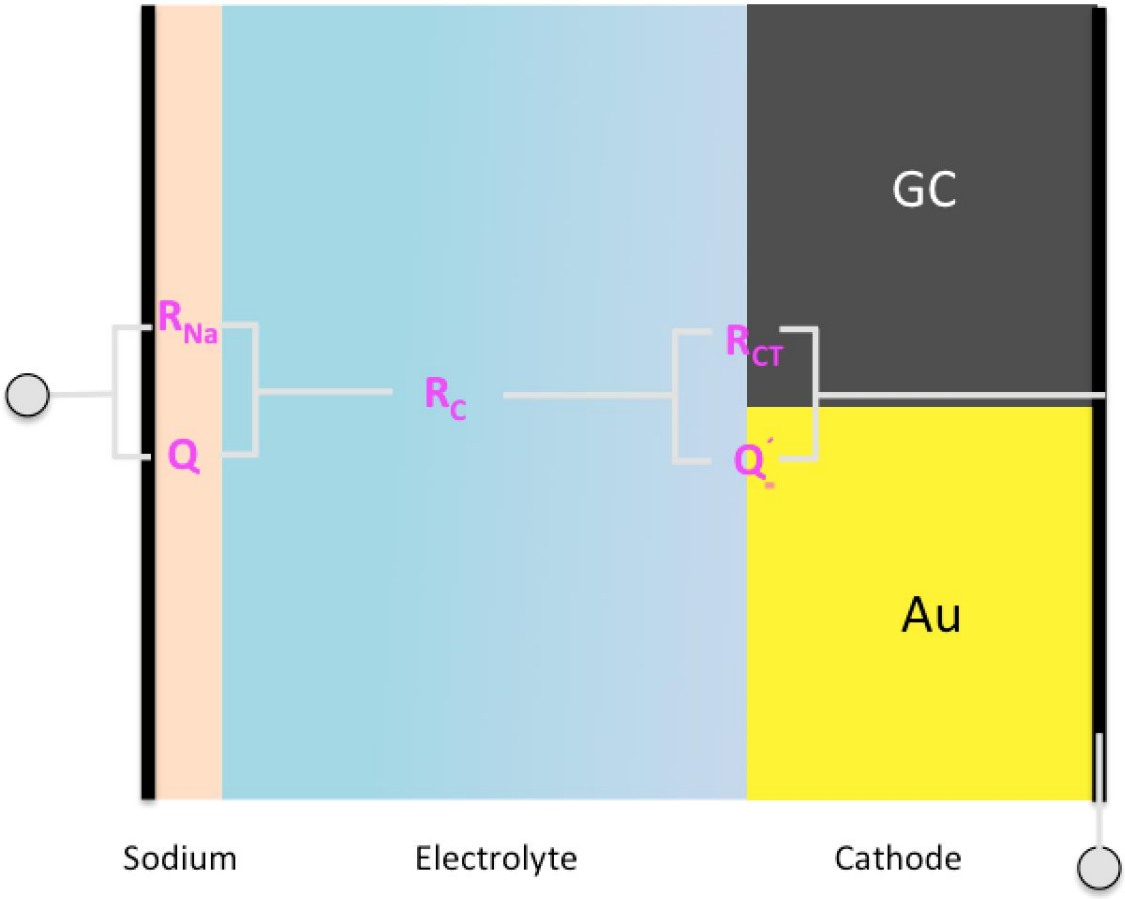

Schematic 1: Representation of the equivalent circuit model, used to fit the planar GC and Au cathode, based on the model described by Knudsen et al.[1] R_C is the electrolyte and cell resistance, R_{Na} describes the charge-transfer resistance occurring at the sodium/electrolyte interface, and R_{CT} charge-transfer resistance at the cathode surface/electrolyte interface, and Q represents a constant phase element describing the double-layer capacitance of the electrode surfaces and interfaces.

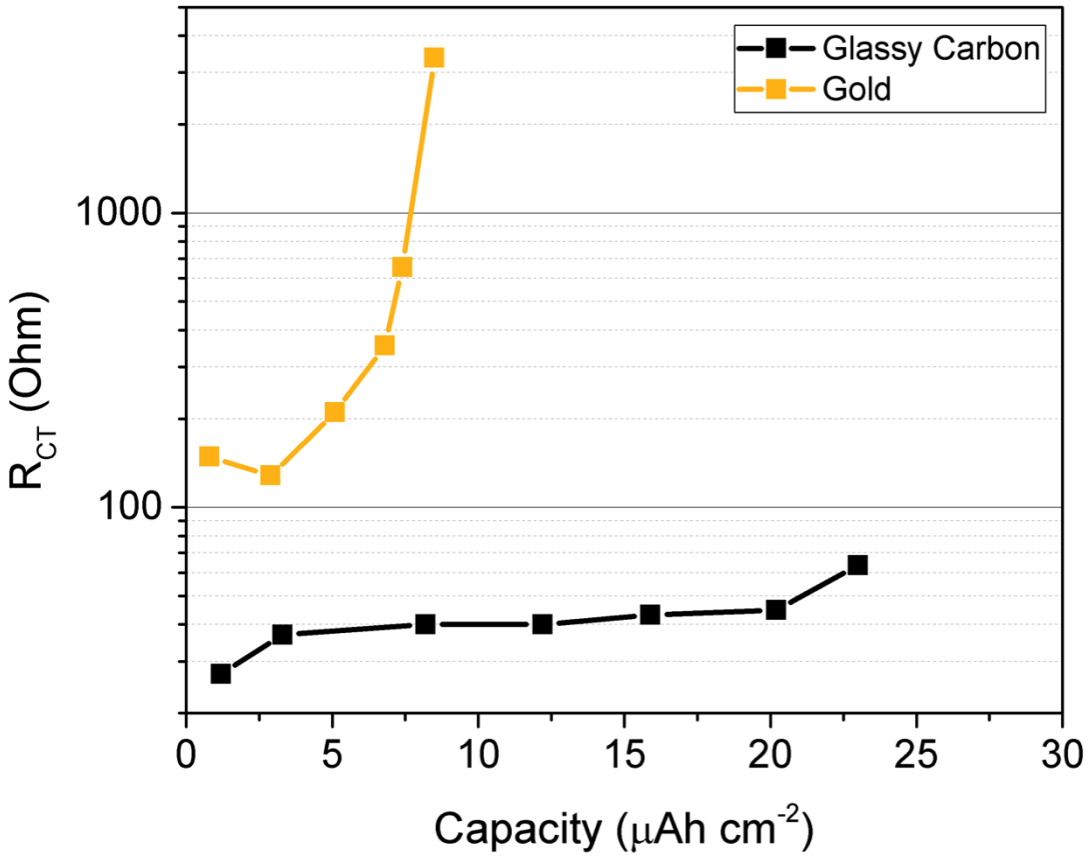

Figure S1: Fitted resistance evolution of charge transfer reaction at the Au (yellow line) and GC (black line) working electrode during discharge at 100 μA/cm^2 in DGME (0.5 M NaOTf).

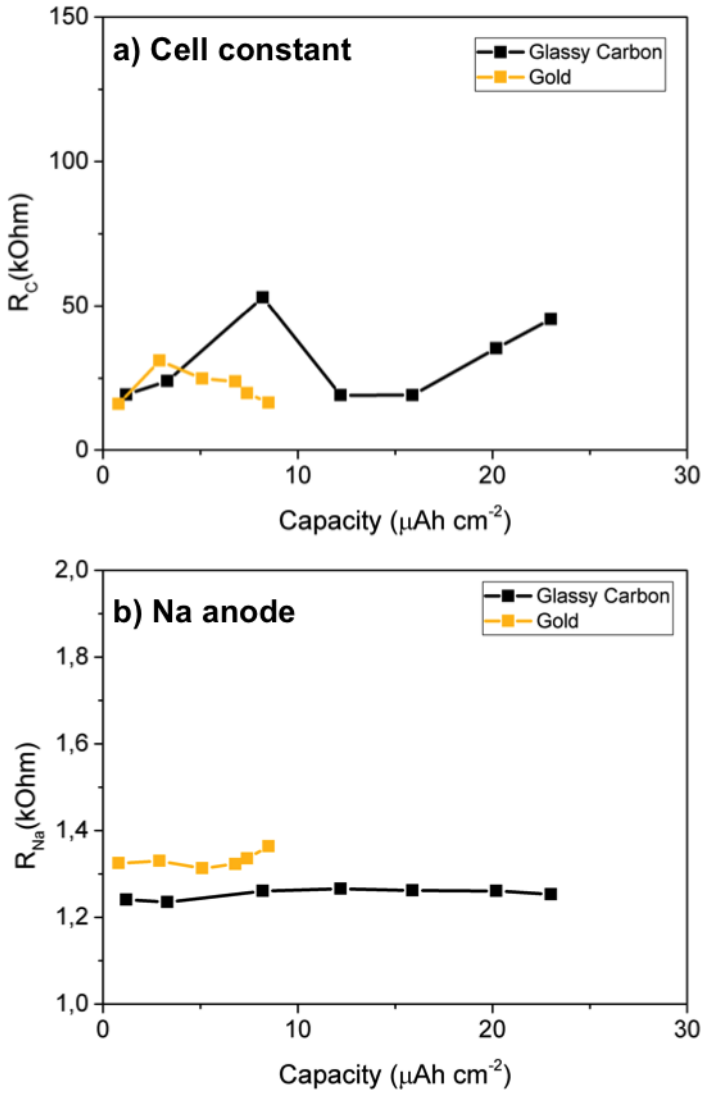

Figure S2: Fitted resistance evolution based on of the cell constant (a) and the Na anode (b) when using an Au (yellow line) and GC (black line) working electrode during discharge at 100 μA/cm^2 in DGME (0.5 M NaOTf).

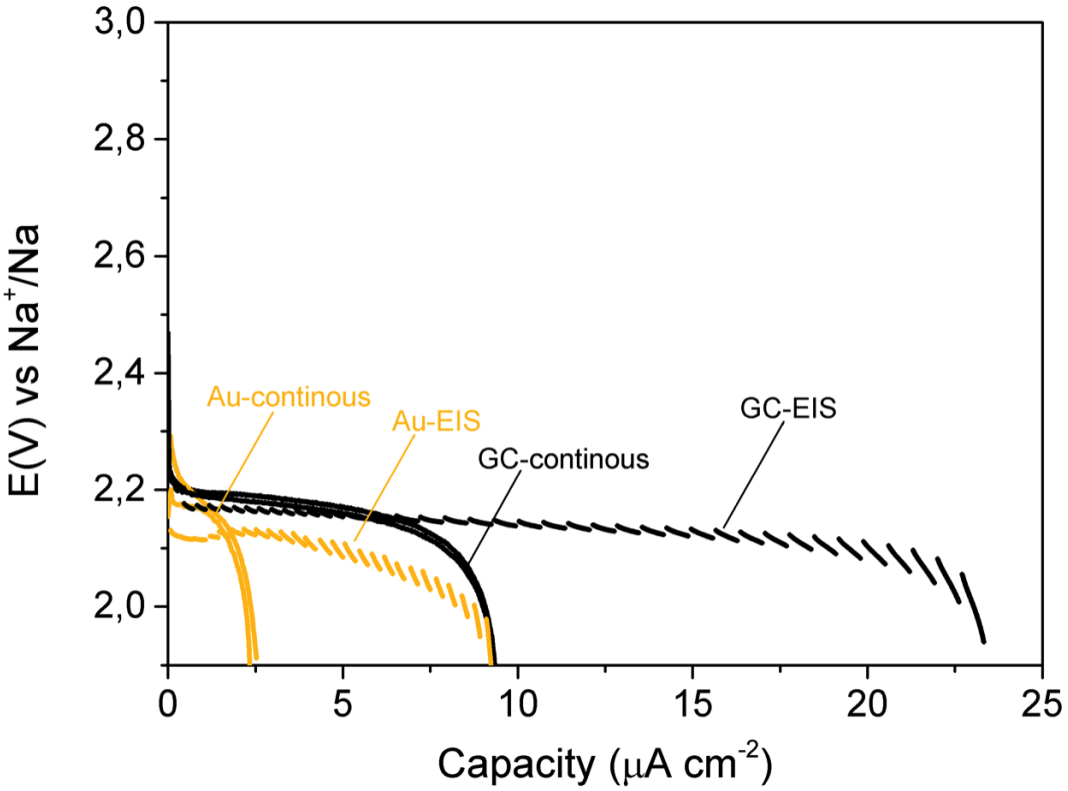

Figure S3: Comparison of discharges on planar Au and GC electrodes in DGME (0.5M NaOTf) 100 μA/cm^2, using Na metal as ref., with (dashed lines) and without impedance intervals (solid lines). Larger capacities in impedance discharges observed due to OCV impedance intervals, allowing for desolvation of NaO_2. It is important to note that the OCV-impedance interval following each discharge period allows for the solvation of NaO_2 into the bulk electrolyte, liberating additional electrode surface for O_2 reduction. Consequently, increased capacities when compared to a constant discharge are consistently obtained by this technique. Nevertheless, the trend is consistent with that obtained in the absence of an OCV hold and GITT measurement; i.e., the capacity at the Au electrode is less than that obtained at the GC electrode (Figure S3).

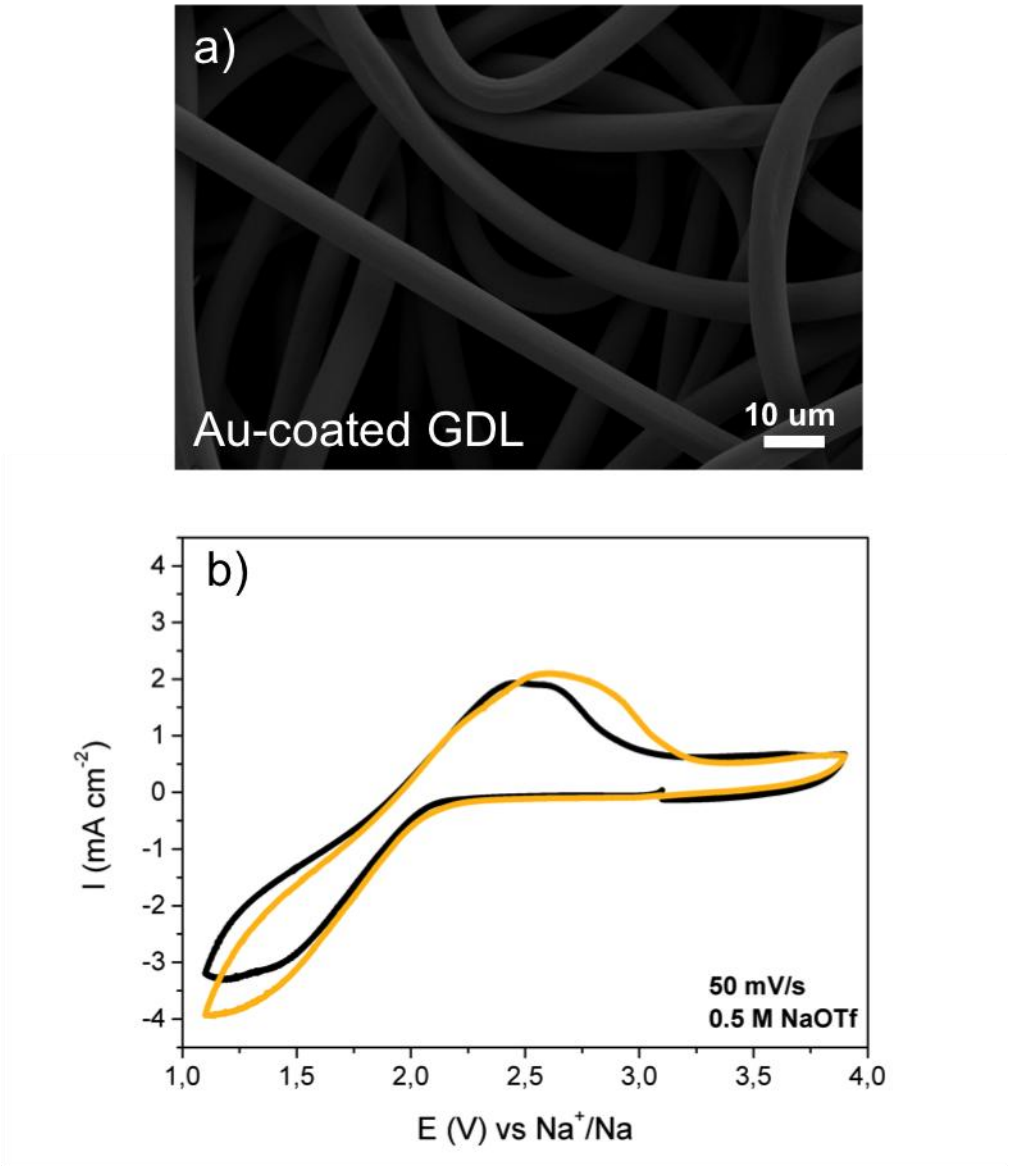

Figure S4: SEM image of Au-coated GDL fibers (20-30 nm) (a). Cyclic voltammograms of oxygen reduction on GDL (black) and Au-coated GDL (yellow) surfaces at 50 mV/s in DGME using 0.5M NaOTf as conductive salt (b).

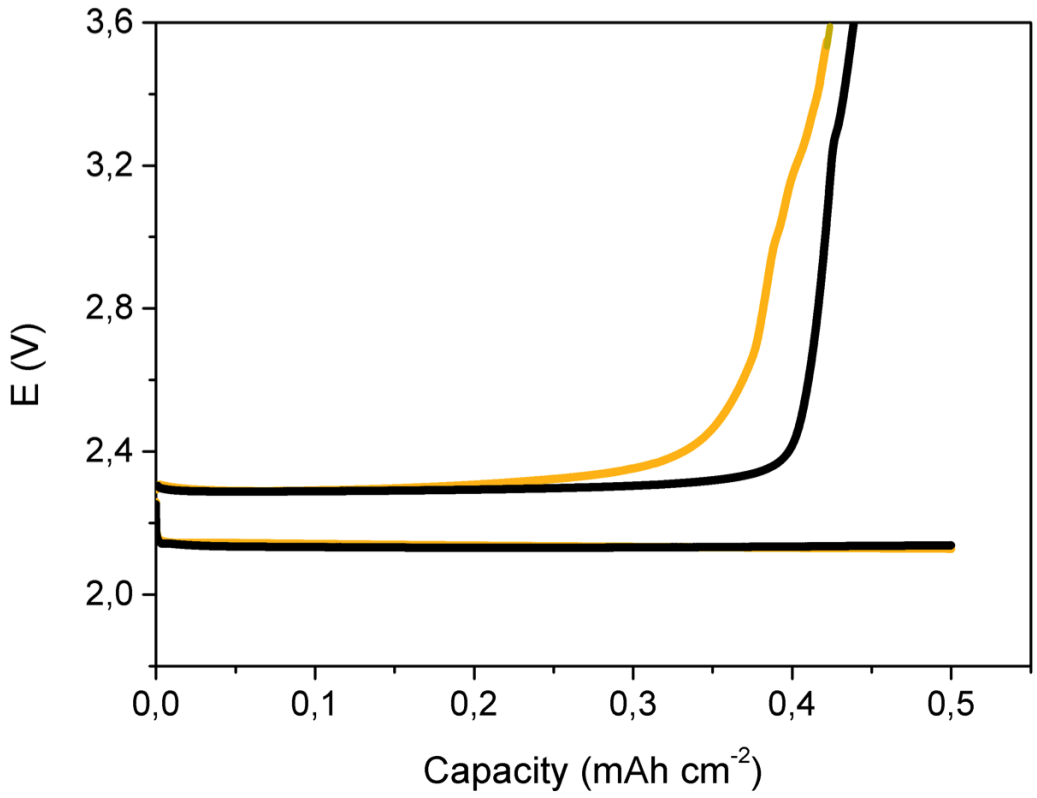

Figure S5: Shallow cycling of a GDL electrode (black line) and Au-coated GDL electrode (yellow line) in DGME (0.5 M NaOTf) at a rate of 25 µA/cm^2.

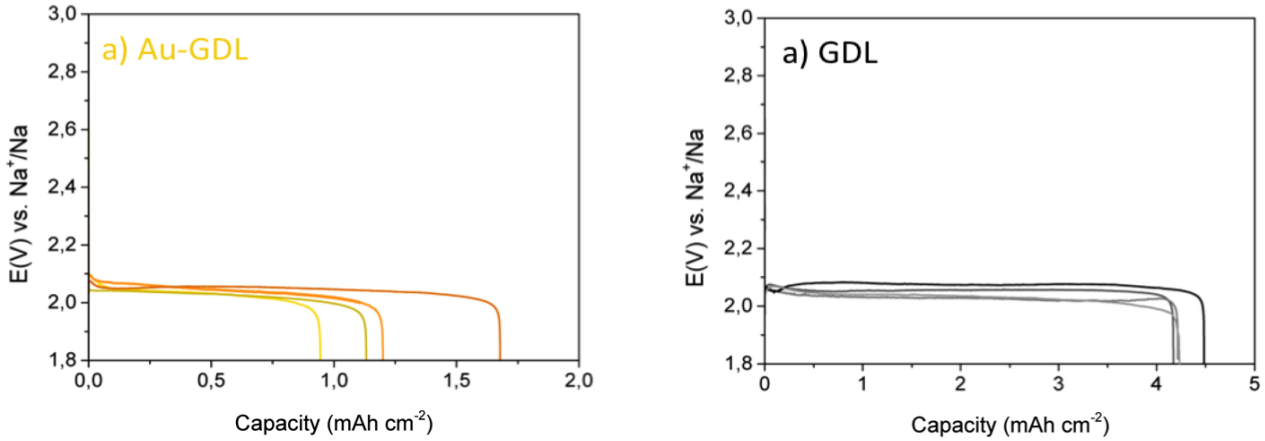

Figure S6: Multiple discharges using an Au-coated GDL electrode (a) and a pristine GDL electrode (b) in DGME with 0.5 M NaOTf, at a rate of 25 µA cm^{-2}.

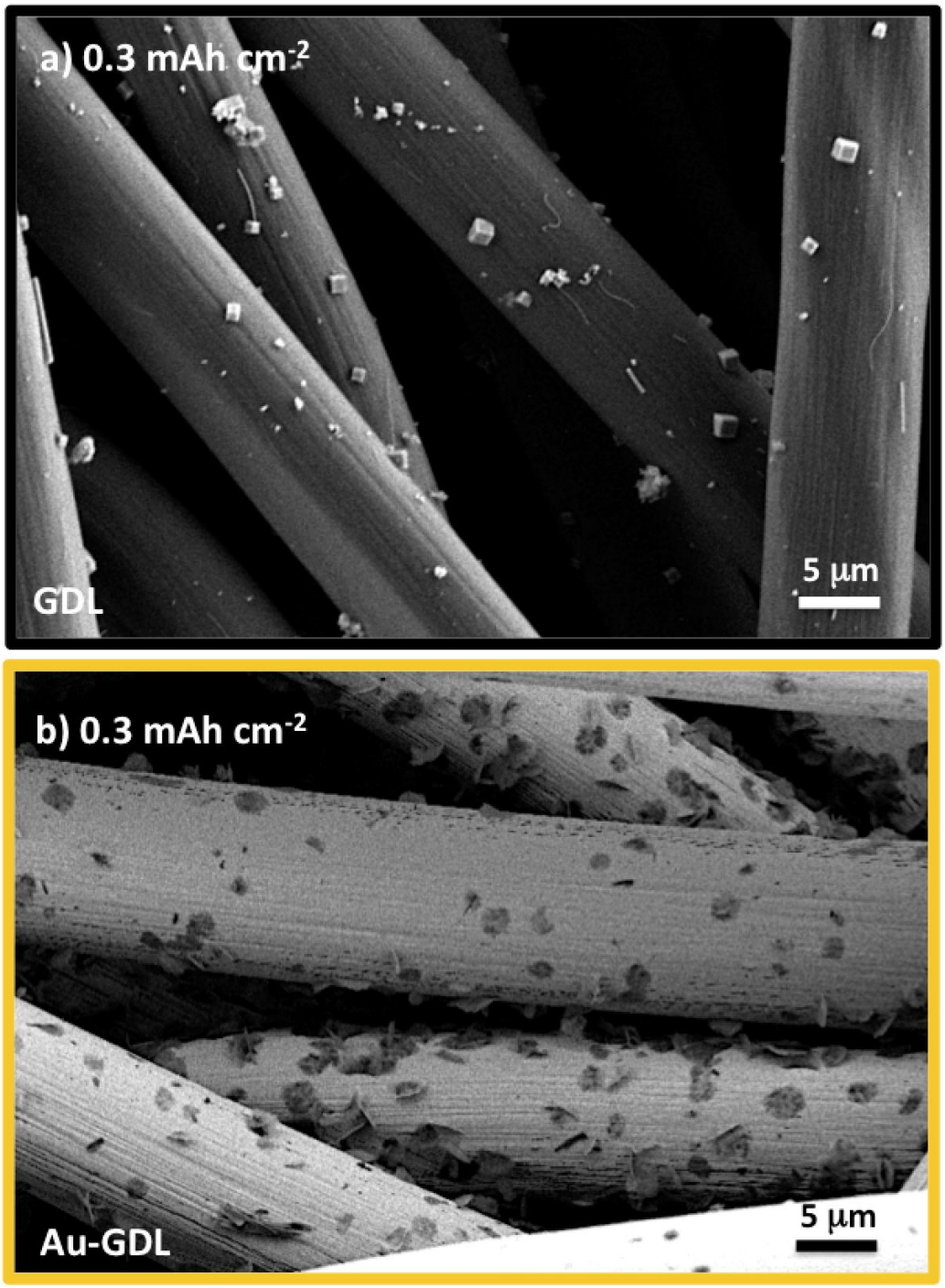

Figure S7: Size distribution of discharge product on GDL (a) and Au-GDL (b) electrodes discharged to 0.3 mAh/cm².

Table S1: Specific surface energies and O_2 affinities for gold and carbon.

Surface	Specific surface energy [mJ/cm^2]	Oxygen affinity [mJ/cm^2]
Gold	0.150 [2]	-2.4 [3]
Carbon	0.004[4] [5]	-0.4 [3]

Specific surface energies for Au and C were obtained from Literature. The oxygen affinities of Au and C calculated by Lu et al.[3] were normalized assuming 10^{16} atoms per cm^2 for Au[6] and 10^{15} atoms per cm^2 for carbon[7]

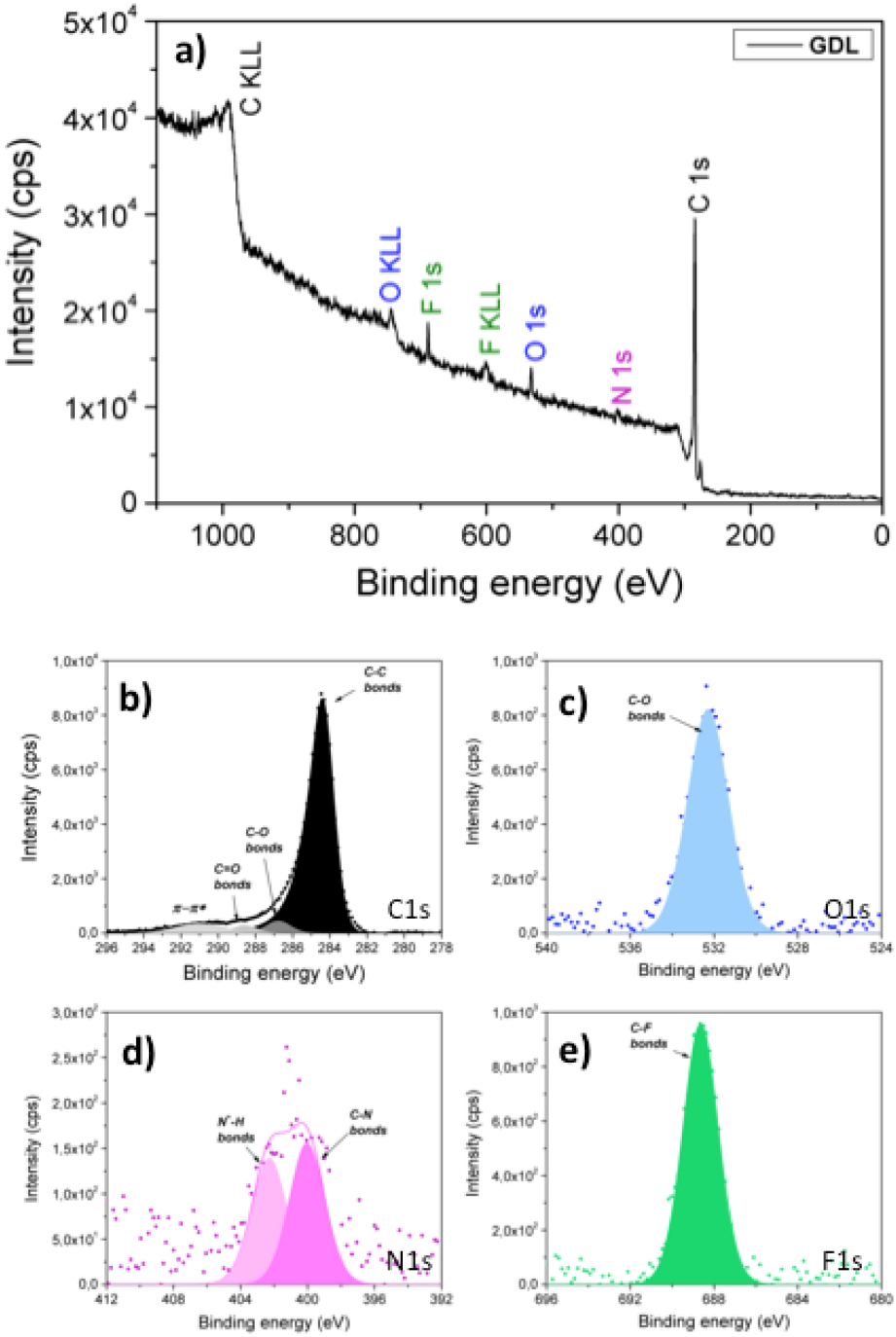

Figure S8: Overview XPS scan of GDL electrode (a). Verification of presence of various surface groups on the GDL fiber in detailed spectra of C1S (b), O1s (c), N1s (d) and F1s (e).

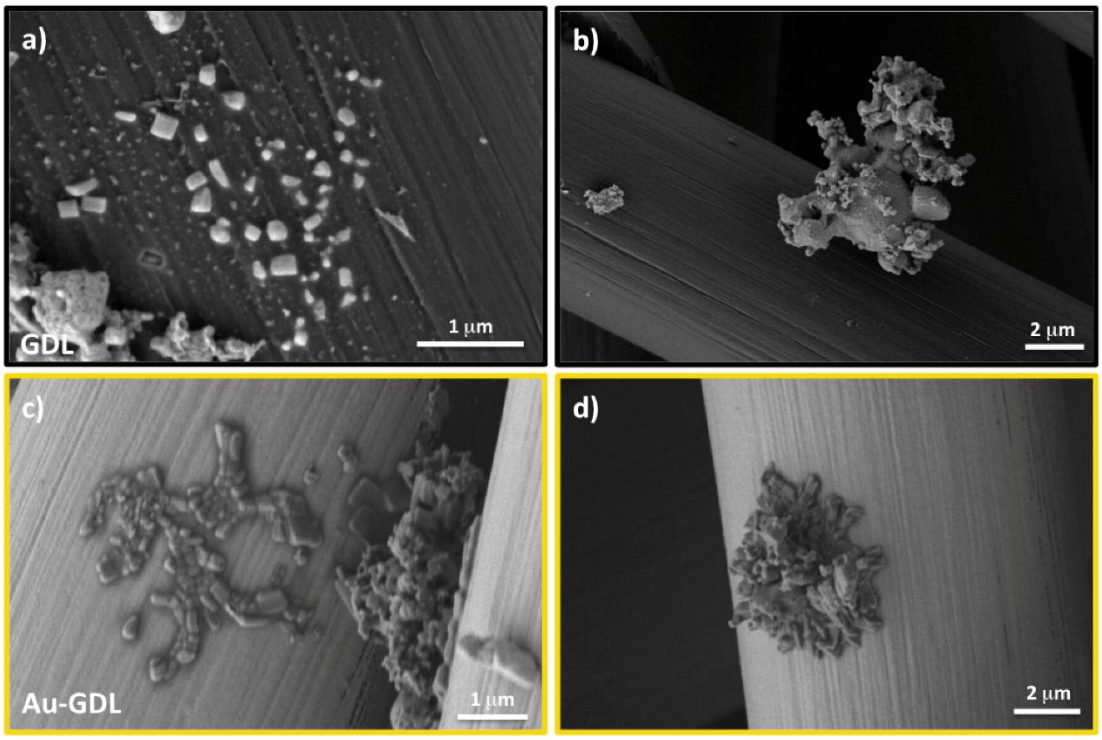

Figure S9: SEM images of chemically precipitated KO_2. Nuclei and growing structures of KO_2 on GDL fibers exhibit small electrode-KO_2 interface areas (a), (b). Island growth of KO_2 on Au-GDL fibers with large electrode-KO_2 interface contact (c), (d). In a glove box, standard GDL and Au-coated GDL were immersed in KO_2 saturated DGME solution (H_2O < 20 ppm) and the crystallization process was allowed to proceed for 48h. Electrodes were subsequently washed with dry DME to remove any unattached product

References:

[1] K. B. Knudsen, J. E. Nichols, T. Vegge, A. C. Luntz, B. D. McCloskey, J. Hjelm, The *J. Phys. Chem.* C., **2016**, *120*, 10799.
[2] L. Vitos, A. V. Ruban, H. L. Skriver, J. Kollar, *Surf. Sci.*, **1998**, *411*, 186.
[3] Y. C. Lu, H. A. Gasteiger, Y. Shao-Horn, *J. Am. Chem. Soc.*, **2011**, *133*, 19048.
[4] W. D. Bascom, L. T. Drzal, *Nasa contractor report 4084*, **1987**.
[5] A. Zebda, H. Sabbah, S. Ababou-Girard, F. Solal, C. Godet, *Appl. Surf. Sci.*, **2008**, *254*, 4980.
[6] S. Bhatia, *Zeolite Catalysis: Principles and Application* CRC Press, Inc. , Florida, USA, **1989.**
[7] J. Fraissard, C. W. Conner, *Physical Adsorption: Experiment, Theory and Applications* Kluwer Academic Publishers, Dordrecht, NL, **1996**.